Supplement of Atmos. Chem. Phys., 26, 15735–15755, 2026
https://doi.org/10.5194/acp-26-15735-2026-supplement
© Author(s) 2026. CC BY 4.0 License.



Atmospheric Chemistry and Physics
Open Access
EGU

Supplement of

CO emissions and NO_x / CO ratios from the extreme 2025 Iberian wildfires: TROPOMI-based estimates and comparison with inventories

Alberto Álvaro-Díaz et al.

Correspondence to: Cristina Prados-Roman (pradosrc@inta.es)

The copyright of individual parts of the supplement might differ from the article licence.

S1 TROPOMI-derived uncertainties

S1.1 Integrated mass enhancement and mole density ratio

Uncertainties of TROPOMI-derived CO emission rates are computed using the error propagation from Eq. (2) and read as follows

$$\Delta E = \left|\frac{IME}{L}\right| \Delta u + \left|\frac{u}{L}\right| \Delta IME + \left|\frac{u \cdot IME}{L^2}\right| \Delta L \ , \qquad (S1)$$

where $IME = M_m \sum_i \Delta\, VCD_i A_i$ and ΔIME is its standard deviation. Δu is the wind speed standard deviation. As discussed in Sec. 4.1.3, the wind speed is obtained by averaging within the hours of the time of the overpass and in altitude up to the PBLH. The uncertainties are manly driven by the wind speed standard deviation. Approximately, it is found that this factor corresponds to 80% of the uncertainty.

Uncertainties for NO_2/CO mole density ratios (MDRs) defined in Eq. (5) are computed using the vertical column density precision provided by L2 TROPOMI. Similarly to Eq. (5), MDR uncertainties are defined as follow

$$\Delta MDR = \frac{\overline{VCD}_{prec,NO_2}}{\overline{VCD}_{prec,CO}} \cdot 10^3 \ , \qquad (S2)$$

where $\overline{VCD}_{prec,gas}$ is the TROPOMI precision variable of the specific gas averaged over the plume pixels. In the scenes investigated in our work, the mean precision on the NO_2 VCD in the plume pixels was ~25-30%. Additional possible uncertainties due to scattering are discussed in the following Sect. S1.2. Also, a sensitivity test assessing the possible effect of the lifetime of NO_x for our NO_x/CO MDR is provided in Sect. S3 of this supplementary.

S1.2 Sensitivity to scattering-related uncertainties in NO_2 retrievals

Our study uses TROPOMI-retrieved NO_2 and of CO VCDs. Each gas is retrieved in a different spectral region (Vis and SWIR, respectively). However, these different spectral ranges also imply different sensitivity of each product towards scattering. Since wildfires emit not only gases but also aerosols, the sensitivity of Vis satellite observations particularly to the low troposphere is limited compared to SWIR observations. These scattering-related uncertainties in NO_2 retrieval could potentially affect our CO and NO_2/CO MDR (and hence NOx/CO MDR) estimates.

Griffin et al. (2021) performed sensitivity tests on TROPOMI NO_2 VCDs and noticed the complex relationship between NO_2 VCDs and aerosol scattering in wildfire scenarios. Outside of the fire plumes, the authors found no particular effect of aerosols on the NO_2 fields. However, they reported 20% uncertainty on the NO_2 air mass factor for in-plume observations. They also pointed out that the effect of scattering on satellite NO_2 observations could either increase or decrease reported NO_2 VCDs, depending on the viewing geometry and aerosol optical depth. In the work of Wang et al. (2026), reporting on monthly mean NO_2 TROPOMI VCDs, the authors performed sensitivity tests on the retrieved NO_2 VCDs using model-derived a priori information containing or not fire-related NO_2 and aerosol information. Their results also indicate that retrieved NO_2 VCDs could be affected by aerosols. If the retrieval considered a priori fire information, Wang et al. (2026) reported NO_2 VCDs differences of up to +60-70% for satellite pixels in- or in-the-edge of a fire plume, and +20% different NO_2 VCDs for background pixels. Since the magnitude of these differences varies between plume and background pixels, their effect on NO_2 ΔVCDs (Eq. 1) would depend on the relative NO_2 VCDs in both regions. Note that, unlike Griffin et al. (2021), conclusions reported by Wang et al. (2026) were not validated against observations. Also, Wang at al. (2026) reported that their observations could be affected by NO_2 emissions from big cities, which is not the case in our work. Therefore, we consider ±20% as probably the more realistic perturbation magnitude and ±50% as a larger sensitivity scenario based on the substantial retrieval differences reported by Wang et al. (2026).

Given our approach for the synergy plume masking and MDRs calculations, the uncertainty on the satellite NO_2 VCDs due to scattering in fire scenes could propagate into our TROPOMI-derived estimates. Scattering could indeed affect directly our NO_2-derived NOx/CO MDRs. Moreover, it could also affect the selection of plume pixels by the synergy method (Sect. 4.1.2) and, hence, our reported CO emission rates. If we consider a spatially uniform systematic bias on the NO_2 fields of e.g. ±20% in the NO_2 VCDs across the whole scene, the synergy plume masking method selects the same pixels, leaving our CO estimates unchanged. In contrast, the NO_2/CO MDRs would change proportionally to the applied bias (i.e., ±20%), as expected from Eq. (5). However, as notice by Griffin et al. (2021), the magnitude and sign of NO_2 retrieval errors due to scattering may vary spatially depending on e.g. aerosol loading or viewing geometry. Since the spatial distribution of these errors is not known for the scenes we investigated, their potential impact on the synergy plume masking method is less straightforward. To assess this, we performed tests by randomly modifying each NO_2 pixel by up to ±20% and ±50%, assuming a uniform probability distribution in the whole scene. In our study, this "whole-scene" scattering uncertainty is probably the most realistic one since most of the wildfires we investigated were surrounded by nearby fires and hence by the possibility of aerosol scattering. Results

shown in Fig. S1 indicate that perturbations of the NO_2 fields have only a small overall effect on the CO emission rates retrieved with the synergy method. However, based on the correlation values (R~0.9 and R=0.6 for 20% and 50%, respectively), the sensitivity of individual scenarios increases as the NO_2 perturbation becomes larger. These results suggest that the synergy masking method applied in our work is robust to moderate NO_2 perturbations, although large perturbations can modify the selected plume pixels and hence affect individual emission estimates (Fig. S1a). The effect of such NO_2 perturbation on the NO_2/CO MDR is shown in Fig S1b. As expected from the MDR formula (Eq. 5), the effect of changing NO_2 VCDs does directly affect the NO_2/CO MDRs values although, given the correlation values, the effect is case-dependent.

Overall, these results suggest that the effect of scattering-related NO_2 uncertainties on our estimates depends on their spatial distribution. While a uniform bias would not affect our CO emission estimates, it would directly propagate into the MDRs. On the other hand, spatial variations in NO_2 VCDs could affect both estimates, although our sensitivity tests suggest that moderate perturbations (±20%) have a relatively small overall impact on the retrieved CO emissions. Although these sensitivity tests do not explicitly simulate aerosol scattering, they provide useful insight into how NO_2 retrieval uncertainties may affect our estimates, particularly since the true aerosol properties and their spatial distribution are not sufficiently known for the fire scenes investigated herein.

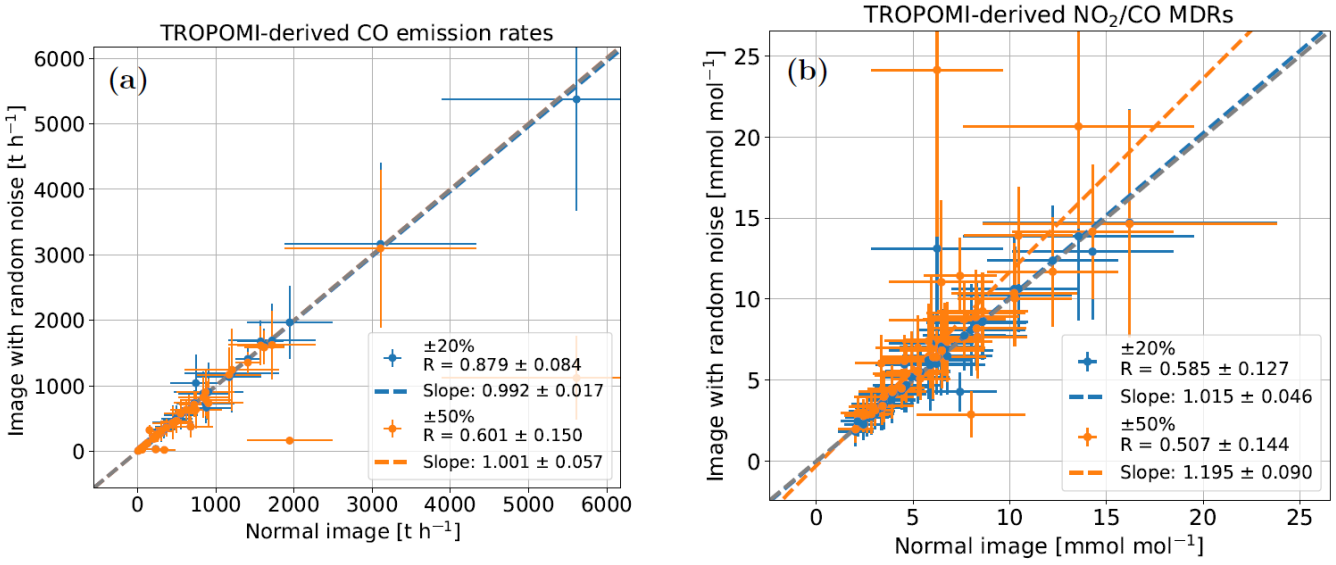


Figure S1: TROPOMI-derived estimates including ±20% (orange) and ±50% (blue) NO_2 VCDs random perturbations in all the pixels of the scene under investigation. (a) CO emission rates. (b) NO_2/CO MDRs. Results are compared to our reference values reported in x-axis. The grey dashed line shows the 1:1 correspondence.

S1.3 Quality assurance pixel value

The quality assurance (qa) value is a pixel-level indicator provided with the TROPOMI Level-2 products to assess retrieval quality, where $qa = 0$ refer to invalid or defective retrievals. Following the work of Griffin et al., (2021, 2024), in this study

we used a quality flag of TROPOMI data of *qa > 0.5* (Sect. 3.1). We tested the algorithm for *qa > 0* to quantify the effect of relaxing this threshold even further. Results are presented in Fig. S2. We find that the *qa* value does not seem to affect the emission rates retrieved.

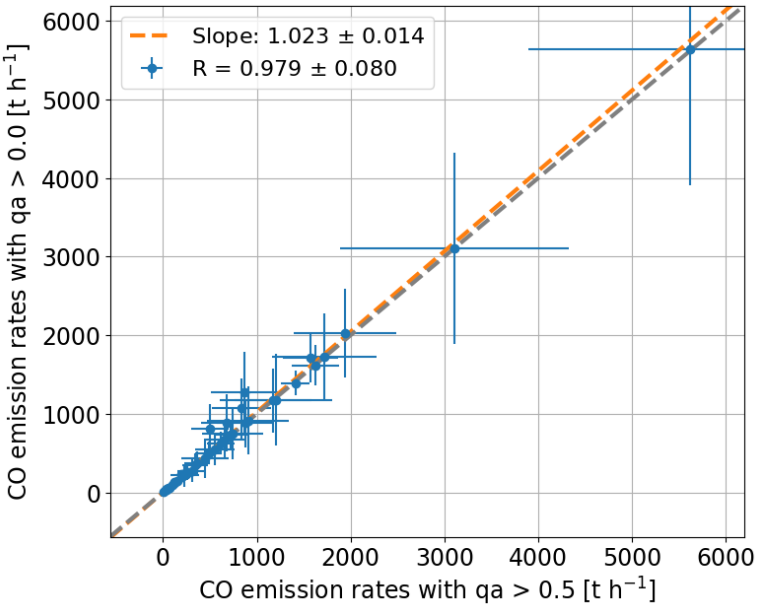


Figure S2: TROPOMI-derived emission rates for quality assurance flag values of *qa > 0* (y-axis) and *qa > 0.5* (x-axis). The grey dashed line shows the 1:1 correspondence, and the orange dashed line represents the linear fit.

S1.4 Other background choices

To assess the sensitivity of our CO emission estimates to the background selection, we compared our results obtained after using the upwind method (Sect. 4.1.1) with those obtained using a fixed regional CO background defined as the mean TROPOMI CO VCD over the broader study area (38–44° N, 9–3° W; i.e, northwest region of the Iberian Peninsula) before the main fire period. This broad area covers all the individual fire regions investigated in our work (Fig. 1 and Table 1). This broad area regional CO VCD background for the pre-fire period (1-31 July 2025) resulted 0.027 mol m^{-2}. Figure S3 compares this fixed value with the scene-specific upwind backgrounds used in the retrievals. During the main fire period, many upwind background values exceed the pre-fire regional mean and, in some cases, the regional daily mean. This indicates that the air entering some target plumes was already enriched in CO, likely due to spatially heterogeneous smoke and transport from other fires.

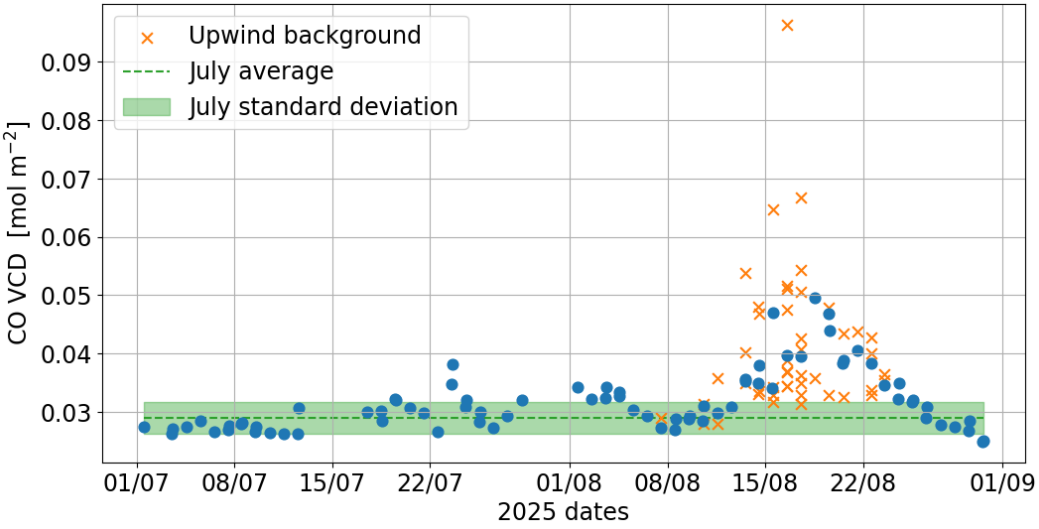


Figure S3: CO regional average temporal evolution in mol m^{-2}. Crosses correspond to upwind background for each scene studied in this work. Green dashed line represents the average value within the months of July 2025 and green shadows represents its standard deviation. Blue dots refer to regional daily means CO VCD.

Figure S4 shows that using the fixed regional background instead of the scene-specific upwind background increases the retrieved CO emission rates by about 39%. This is consistent with part of the pre-existing CO being attributed to the target fire when a fixed background is used, supporting the use of the upwind approach in these complex multi-fire conditions.

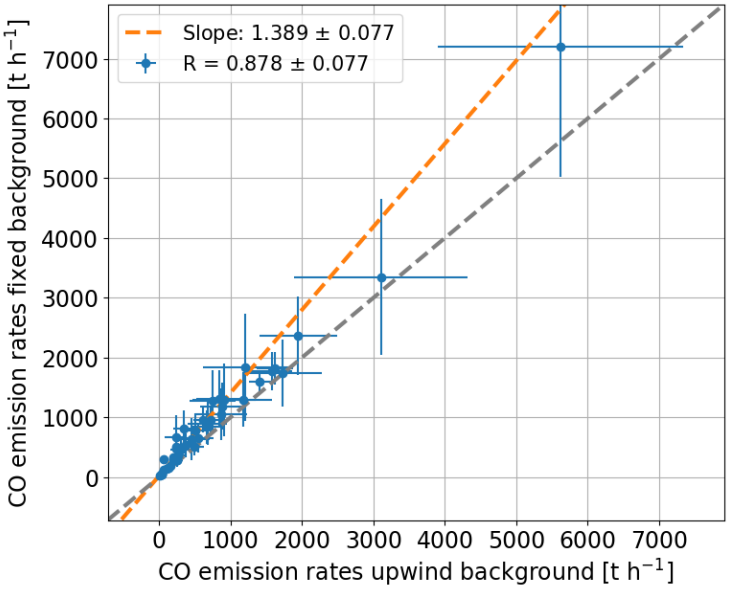


Figure S4: TROPOMI-derived CO emission rates for upwind background (x-axis) and fixed background 0.027 mol m^{-2} (y-axis). The grey dashed line shows the 1:1 correspondence, and the orange dashed line represents the linear fit.

To further assess the sensitivity of our CO emission estimates towards the background selection, we investigate the possible effect of the size of the background region considered. As detailed on Sect. 4.1.1, the reference size of the background region used in our work is 0.8° x 0.6°. We repeated the calculation of the CO emission rates using a background with twice the dimensions of the reference region (1.6° × 1.2°) and also with half the dimensions (0.4° × 0.3°). As shown in Fig. S5, despite this large change in chosen size of the background area, the retrieved CO emission rates remain generally consistent with our reference estimates. Linear regressions against the reference case yield slopes of 1.043 for the larger background and 0.970 for the smaller background. The corresponding correlations are also very similar (R = 0.883 and R = 0.885, respectively). Although some individual cases, particularly the largest emission events, seem more sensitive to background selection (~20% in the case of double size), these results indicate that the retrieved CO emission rates do not exhibit a strong systematic dependence on the chosen background dimensions and results are within wind-driven emission uncertainties shown as error bars in Fig. S5.

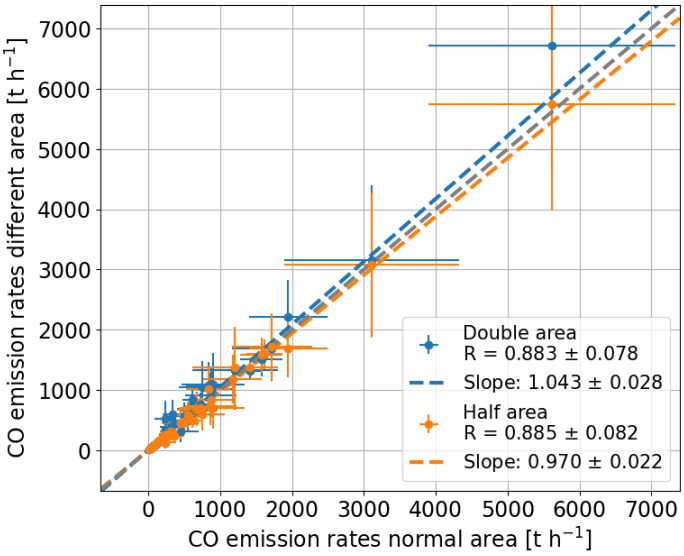


Figure S5: TROPOMI-derived CO emission rates for the reference background dimension (x-axis) and for double (in blue) and half (in orange) that background size (y-axis). The grey dashed line shows the 1:1 correspondence. The dashed lines represent the different linear fits

S1.5 Other sources of uncertainties

Here we describe qualitatively other possible sources of uncertainties in TROPOMI-based estimates.

Since wildfires can spread over several square kilometres, it can be complex to consider a specific and unique hotspot. Moreover, due to the temporal evolution of a wildfire, this hotspot location could evolve as well. The evolution of the burned area, and therefore the consideration of the hotspot, could be taken into account in two different aspects. As discussed in Sec. 4.1.3, the IME method uses the plume pixels and the wind speed. Indeed, the distance of the plume pixels with the hotspot location could affect the plume area variable in Eq. (2). Given its lifetime, for CO we believe this uncertainty does not have an important effect. However, it could be important if NO_2 emission rates were to be computed since the distance from the hotspot is used as variable in Eq. (2) (Griffin et al., 2021).

Moreover, uncertainties on the hotspot location could result in uncertainties on the wind speed selection. As discussed in Sec. 3.3.1, we used the ERA5 wind field nearest to the hotspot. Evolution of the burned area and hotspot location could change the ERA5 coordinate selection and therefore the wind speed used in Eq. (2). Since ERA5 has a spatial resolution of 0.25°, corresponding to roughly 25 km in this region, wind speed can vary substantially between adjacent ERA5 grid points due to e.g. orographic effects. Another ERA5-related uncertainty is the plume injection height. In our study, plume transport is represented by ERA5 winds averaged from the surface to the planetary boundary layer height (PBLH). This choice provides an effective transport wind representative of the boundary layer, where most of the observed smoke is expected to be transported. However, the effective transport level may vary between fires and also depends on the complexity of the terrain, which might not be well represented in the 0.25º ERA5 spatial resolution. To assess the sensitivity of our inferred CO emission rates to this vertical choice, we repeated the calculations using winds averaged from the surface to half the PBL height (PBLH/2) and from the surface to twice the PBL height (2×PBLH). Results are shown in Fig. S6. Overall, extending the averaging layer beyond the PBLH generally includes somewhat higher wind speeds and a larger vertical variability of the wind field. Since the wind-speed standard deviation is propagated into our CO emission rate uncertainties, this is also reflected in the larger error bars obtained for some of the 2×PBLH estimates. In general, this suggests that our inferred CO emissions show limited sensitivity to the assumed vertical transport layer, with no large systematic change over the range tested.

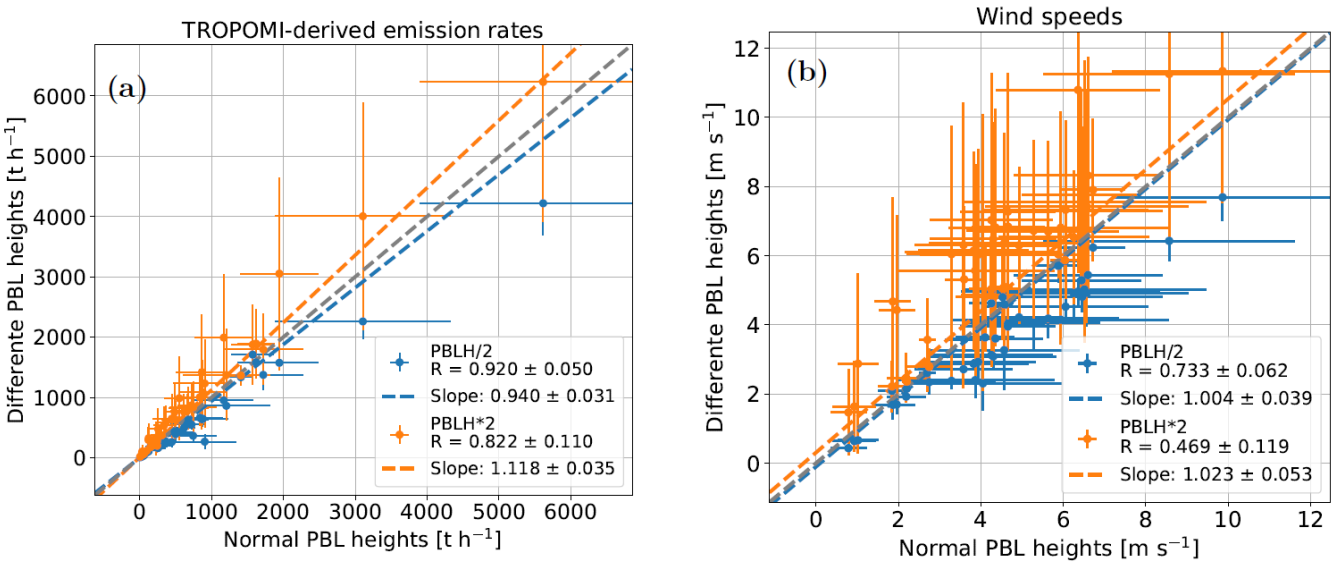


Figure S6: Effect of the altitude injection on (a) the TROPOMI-derived CO emission rates and (b) on the wind speeds. Results are compared to estimates using the reference PBLH.

S2 Plume masking methods

S2.1 Standard threshold method

This standard plume masking method is based on selecting the plume as those pixels which represent an anomaly respect to a specific background (Finch et al., 2022; Lauvaux et al., 2022; Schuit et al., 2023). In our study, we select that background by fixing the region around the point of interest within 1.5° or roughly ±150 km from the hotspot. An anomaly from the background is considered when the value of a TROPOMI pixel is larger than a fixed threshold value (t). This is computed according to

$$\boldsymbol{t} = \boldsymbol{\Delta} VCD_{mean} + \boldsymbol{n} \cdot \boldsymbol{\Delta} VCD_{std} \ , \qquad (\boldsymbol{S3})$$

where ΔVCD_{mean} and ΔVCD_{std} correspond to the mean and standard deviation of the column of the background region once the background is subtracted (Eq. 1). In our work, the NO_2 the threshold plume masking the parameter n in Eq. (S3) is set in the range of $n = 3.5 - 5.5$, although larger values can be set for specific scenarios. Previous studies used lower values (Huang and Wang, 2026). We chose stricter values due to the complexity of the scenes investigated. A specific value within the range mentioned is selected for each case addressing the complexity and coherence of each plume.

Although this standard threshold method worked well for a few of the scenes analysed in this work, depending also on the wind conditions, its performance was limited in cases where several fires co-existed nearby within the same scene. In these

cases, the plume assigned to a given hotspot by this standard method, could include mixed contributions from neighbouring fires. Thus, we suggest a stricter plume masking method called "synergy method".

S2.2 Assessment of synergy plume masking method

As mention in Sec. 4.1.2, in this study a two-step plume masking synergy method was introduced in order to facilitate the identification of individual plumes in our top-down approach. Throughout our work, the standard plume masking method is only used for isolating NO_2 plumes with the intention of later applying it to CO to the synergy plume masking method. However, aiming at assessing this synergy method, herein we applied the threshold method also to the CO fields in the case of simple scenes available (i.e., scenes with one hotspot not surrounded by other nearby fires). In Fig. S7 we compare the CO emission rates retrieved with the synergy method to those inferred using the standard threshold plume masking method on the CO fields. As can be seen, estimates of CO emission rates under simple scenes are quite similar in magnitude and variability.

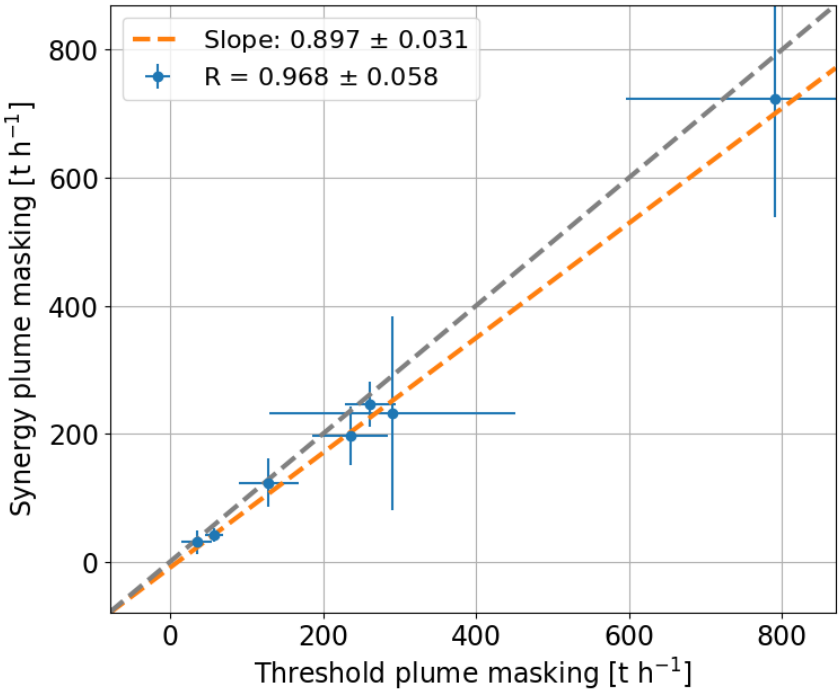


Figure S7: Correlation study of the CO TROPOMI-derived emission rates between both plume masking methods used in this work: synergy and standard threshold. In this plot, only clear and simple fire scenarios are considered. The overpasses used for this plot are shown in Fig. S15. The grey dashed line shows the 1:1 correspondence and the orange dashed line represents the linear fit.

In such simple scenes, the wind and fire conditions facilitate the isolation of the investigated hotspot plume regardless the plume masking method. The simple scenes considered in Fig. S7 are shown in Fig. S15 with the two-step plume masking synergy method for the overpasses for point of interests #1, #5 and #9. This comparison suggests that, at least, for simple scenes, both methods provide similar results. The correlation found is consistent with a relevant R ~ 0.97, with the synergy method yielding lower CO emission rate values (10 %). Note that, as shown in Fig. S15, the synergy method generally selects fewer plume pixels than the standard threshold method because the synergy plume mask is constrained by the shorter-lived NO_2 field.

Another source of uncertainty relates to the chemical differences of NO_2 and CO within a fire plume. Due to the different chemical lifetimes of CO (weeks to months; Novelli et al., 1998) and NO_2 (4-8h; Beirle et al., 2011), the NO_2 plume and the CO plume might not be identical. Sharper gradients are expected for NO_2 close to the hotspot and CO could be transported further from the source as shown in Figs. 3 and 4. Also, since NO_2 is a reactive tracer (Krol et al., 2024), its plume may have a different shape than CO's plume. Thus, with this masking method we might be missing pixels older or more smoldering parts of the plume for the CO emission estimations. In order to assess the effects of this limitation, we investigated the effect on CO emission rates depending on the chosen distance from the source fire (i.e., selected plume area). We applied the standard threshold plume masking method to CO with a distance threshold. We slightly modified the standard threshold plume masking method to be limited up to a specific distance from the source and studied the emission rates as a function of this distance variable. A similar procedure has been applied by Griffin et al., (2024), finding similar results. We chose a simple scenario located at #1, where the synergy and standard threshold approach provided similar emission rates (Fig. S7). The results found are shown in Fig. S8, where it is found that the emission estimates retrieved using the standard threshold approach seems to converge to a constant value with increasing distance. In Fig. S8 the estimated emission (and uncertainty) using the synergy approach is shown as a grey block, indicating that the synergy method is consistent with the standard threshold approach if the plume masked is large enough.

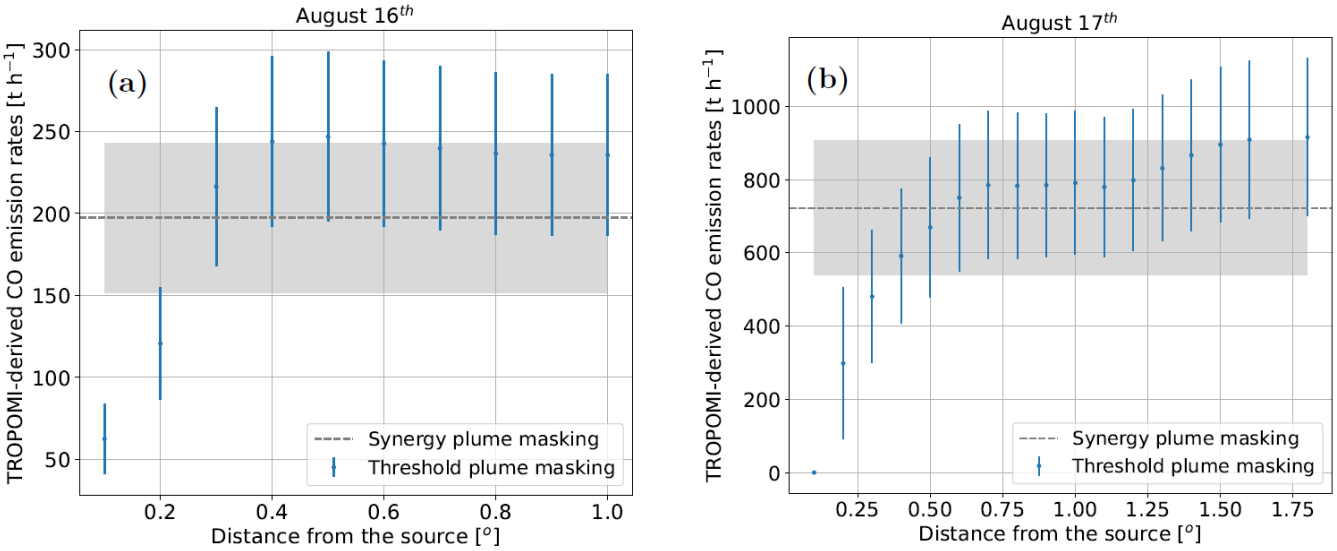


Figure S8: Standard threshold plume masking method applied to compute emission rates (t h^{-1}) as a function of the distance from the source at #1 (a) day 16th, (b) day 17th. In both panels the synergy plume masking method is also shown as a grey block.

As discussed previously, the synergy plume method provides slightly lower emission rates than the standard threshold plume approach. As Fig. S8 shows, this fact does not seem to influence the emission estimates as long as the synergy plume reaches a distance similar where the standard threshold reaches the stability. In the investigated cases, this stability is reached around a distance between 0.4 - 0.6°. For this region, this distance corresponds approximately to 40-60 km away from the hotspot, similarly to the work of Griffin et al., (2024). In Fig. S17 we show the standard threshold plume masking as a function of distance applied at #1 on 17th August 2025 used to compute Fig. S8b. Additionally, Fig. S11 shows the daily evolution of the background-corrected CO fields after applying the synergy plume masking threshold.

Furthermore, due to the differences of the chemical lifetimes, for complex scenarios, with varying wind fields and final stages of the fire (when it is expected that less NO_2 is emitted due to smoldering), the NO_2 density is spread over an extended area causing the synergy method to break down. Only one example was found in this work and is shown in Fig. S9.

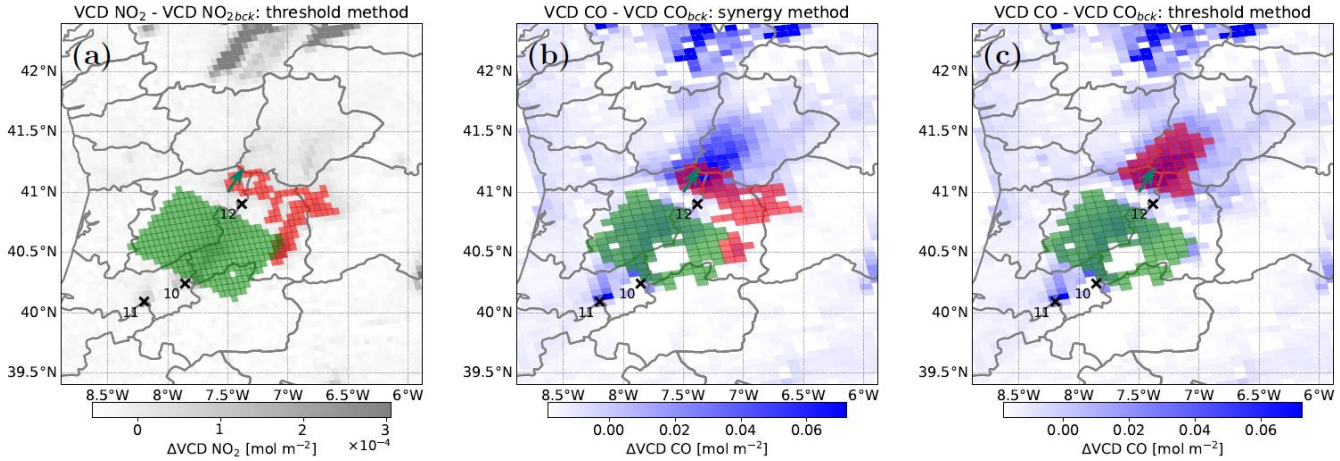


Figure S9: Representative failure of the synergy method. CO TROPOMI background corrected overpasses on 16th August 2025. (a) NO_2 standard threshold plume masking method applied at point of interest #12. (b) CO synergy plume masking method applied at point of interest #12. (c) CO standard threshold plume masking method applied at point of interest #12.

S3 Effect of NO_x uncertainties on TROPOMI-derived NO_x/CO MDR

As detailed in Sect. 4.3, based on previous studies, in our work we use a factor 1.3-1.5 to scale from NO_2/CO MDR based on TROPOMI observations, to satellite-derived NO_x/CO MDRs. The uncertainty associated with this factor is primarily systematic, as different scaling factors would shift the NO_2-derived NO_x/CO MDRs proportionally. To assess the potential impact of this uncertainty, we also tested our NO_x/CO results shown in Fig. 12 and Fig. 13 but using a wider NO_2-to-NOx scaling factor (between 1 and 2). Results, shown in Fig. S10 and Fig. S11, indicate that considering a wider range of scaling factor increases the spread of the satellite-derived MDRs but does not alter the main result reported on Sect. 4.3: TROPOMI-derived NO_x/CO MDRs remain generally lower than those from the inventories. This suggests that the systematic offset found in our work cannot be explained only by uncertainty in the NO_2-to-NO_x conversion factor. Similarly, for the two selected fire events investigated in Fig. 13, we applied the same wider NO_2-to-NO_x factor (Fig. S11). This broader scaling-factor range increases the uncertainty of the TROPOMI-derived NO_x/CO MDRs, without substantially changing their temporal evolution or their difference from the inventories.

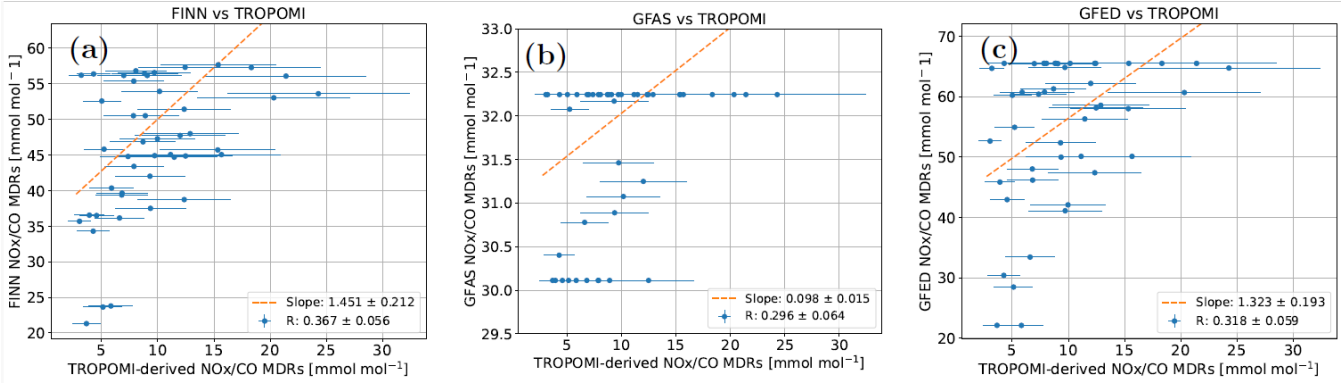


Figure S10: Inventory NO_x/CO MDRs (a FINN, b GFAS, c GFED) against TROPOMI-derived NO_x/CO MDRs. The TROPOMI data correspond to MDRs applying a NO_2-to-NOx factor of 1.5. The error bars in the TROPOMI data cover the 1-2 range for the NO_2-to-NO_x factor.

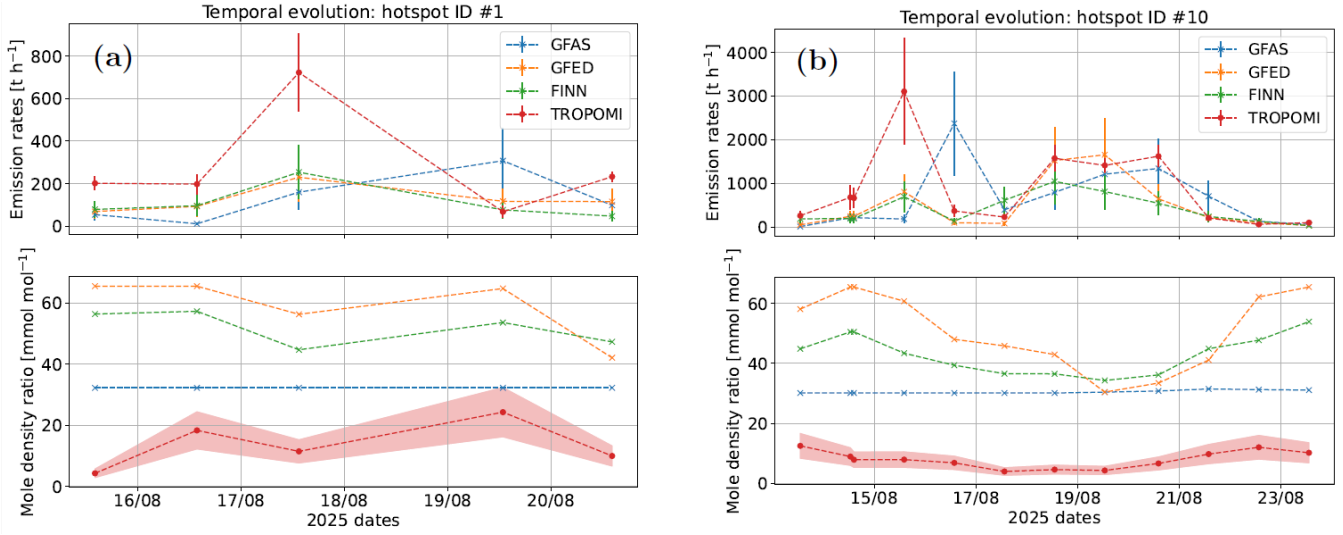


Figure S11: Temporal evolution of two wildfires for different hotspots. (a) #1 (Jarilla) covering 5 days and (b) #10 (Arganil) covering 11 days. Top panels show the CO emission rates (t h^{-1}), while in lower panels show the NO_x/CO MDRs. TROPOMI-related values are shown in red, GFAS' in blue, GFED's in orange and FINN's in green. The red shadow of lower panels corresponds to the TROPOMI NO_x/CO MDR using different NO_2-to-NO_x conversion factors (from 1 to 2).

Additional uncertainties related to NOx estimates is its lifetime within a fire plume. The different lifetime of NOx compared to CO, could potentially affect the interpretation of our NO_2-derived NOx/CO MDR (Eq. 5), since NOx may be progressively removed as the plume ages while CO is comparatively long lived. To assess whether this introduces a systematic effect, we recalculated the NOx/CO MDRs using only half of the pixels of the plume, those closest to the fire (i.e., fresh plume) and compare with MDRs obtained from the reference values using the whole plume. The resulting regression (Fig. S12) has a slope

of ~1, indicating only a slight tendency towards higher MDR values closer to the source, as would be expected from progressive NOx loss downwind. However, no significant systematic effect of plume ageing on the MDR is detected at the spatial scales considered in this study. The moderate correlation between the two cases (R = 0.5, Fig. S12), indicates that the response to restricting the plume extent depends on the specific fire. Overall, these results suggest that the finite NO_x lifetime does not introduce a substantial systematic bias in the MDR values reported in our work.

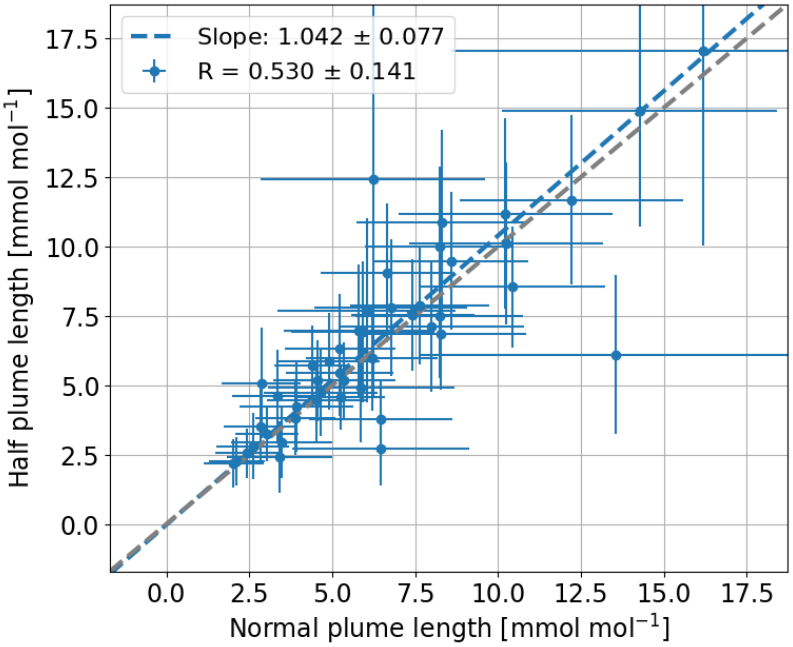


Figure S12: TROPOMI-derived MDR using different plume lengths. The x-axis refers to our reference MDR values using the whole plume length, and y-axis refers to MDRs considering only the part of the plume closer to the fire.

S4 Effect of the different spatial resolution of inventories and TROPOMI observations

As detailed in Table 2, TROPOMI ground pixel and inventories spatial resolution are quite different. However, through our work, estimates derived from both types of sources are compared. Although this different spatial resolution is unlikely the reason behind the discrepancies found between inventories and TROPOMI-reported estimates (Sect. 5.1.3), herein sensitivity tests focus on the two regions we investigated where fires were closer to each other: Galicia and Zamora–León. Note that, given the proximity of the different fires in these regions, the possible effect of the spatial resolution on the different estimates should be most noticeable. First, we compare the CO emissions reported by the finest-resolution inventory (FINN; 1 km x km)

and those provided by the inventory with the coarser spatial resolution (GFED; 0.25°). Results, shown in Fig. S13), indicate that despite the large difference in spatial resolution, the two inventories remain very strongly correlated within these regions (R~0.9). Their regression slopes are 1.188 and 1.521, respectively (i.e., GFED values are in general higher than FINN's), indicating that spatial aggregation may affect the attribution and magnitude assigned to individual neighboring fires, particularly in Zamora–León, but does not substantially reduce the inventory–inventory correlation.

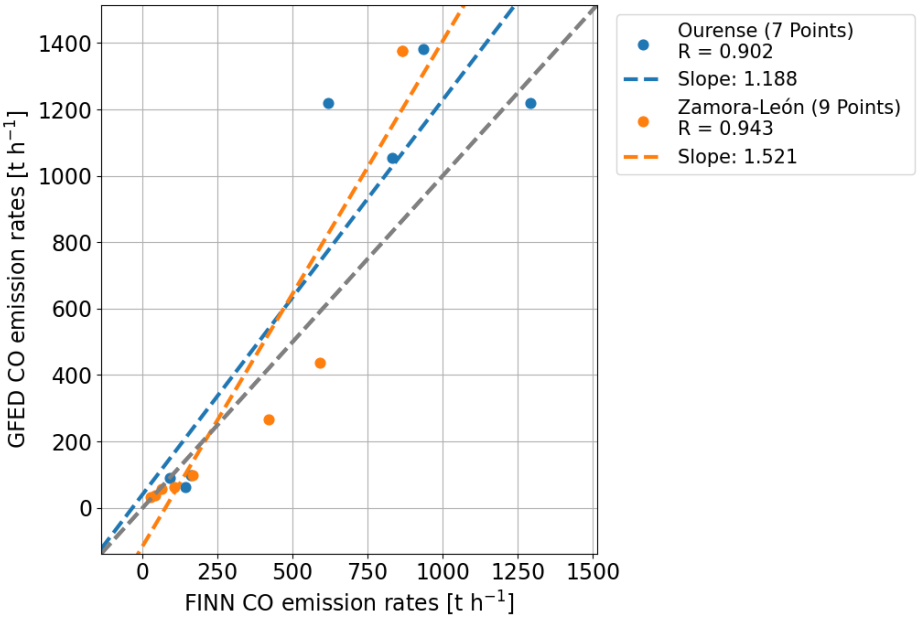


Figure S13: CO emission rates derived from GFED and FINN inventories. Only fires in the region of Galicia (purple) and of Zamora-León (green) are considered. The dashed 1:1 grey line represents is included as reference.

If we compare CO emission estimates on these same regions from both inventories, with estimates from TROPOMI (Fig. S14), the TROPOMI–inventory correlations remain low: R = 0.44 and 0.64 for TROPOMI–FINN, and R = 0.52 and 0.58 for TROPOMI–GFED, for Galicia and Zamora–León, respectively. Note, however, that no systematic improvement is found when TROPOMI is compared with the higher-resolution FINN inventory rather than with GFED (in fact, similar R values are found as for study presented in Fig. 9).

These results suggest that, indeed, the spatial resolution may introduce uncertainty in the attribution of emissions to individual fires, particularly in complex multi-fire situations. However, the spatial resolution alone is unlikely to drive the weak TROPOMI–inventory correlations.

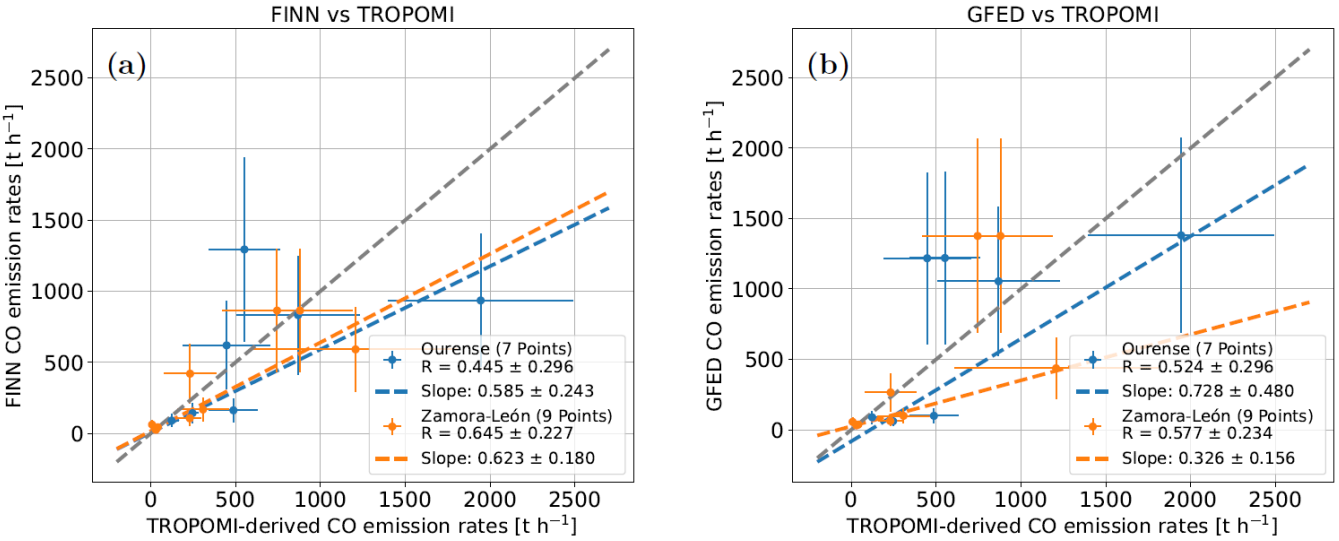


Figure S14: CO emission rates derived from TROPOMI and from FINN (upper) and GFED (bottom) inventories. Only fires in the region of Galicia (purple) and of Zamora-León (green) are considered. The dashed 1:1 grey line represents is included as reference.

S5 Supplementary figures

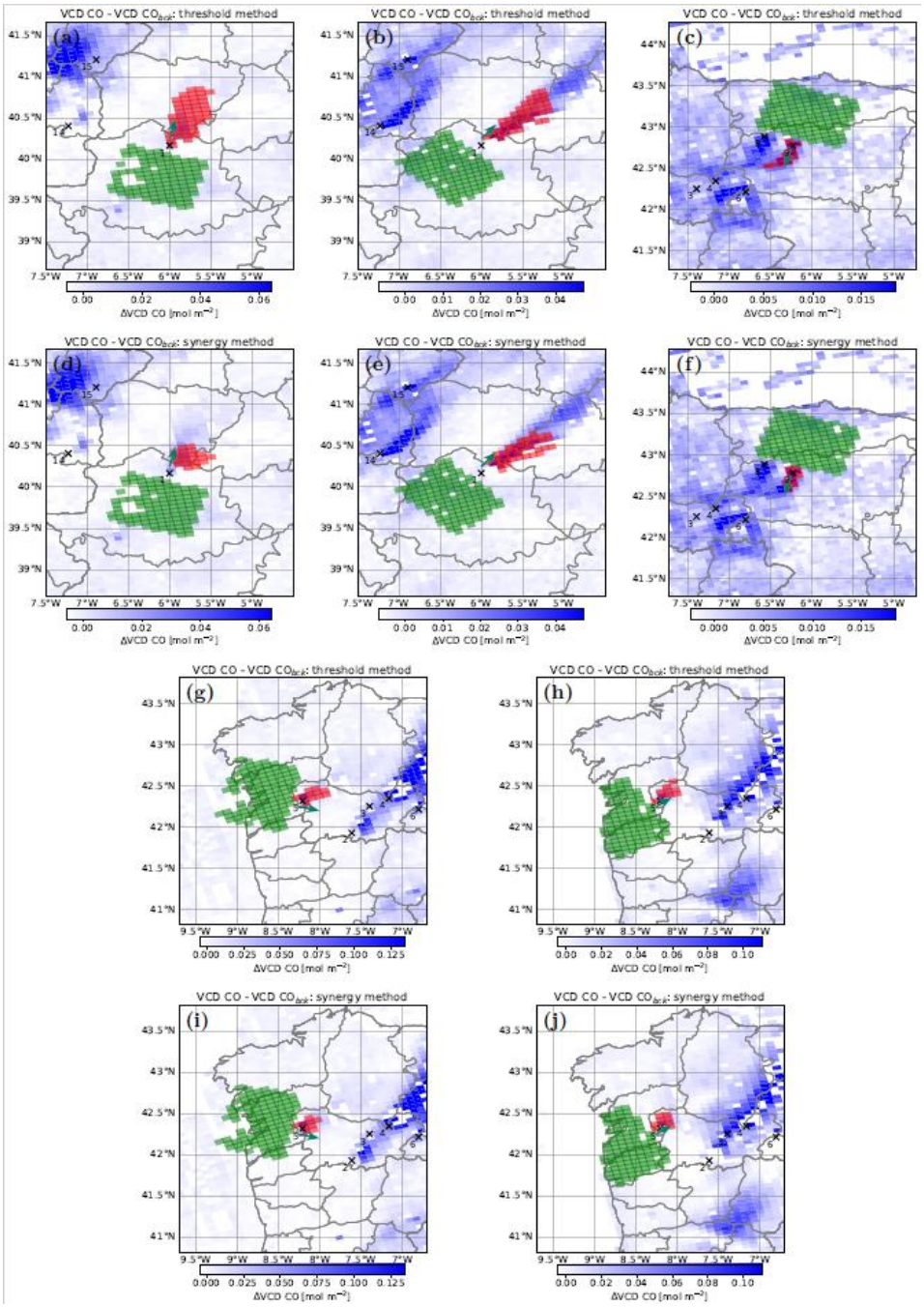


Figure S15: Background-corrected CO VCD maps (ΔCO) for easy scenes using standard threshold plume masking method and using the synergy approach. (a) and (b) standard threshold approach and (d) and (e) synergy approach applied at site #1 on 16th and 17th respectively. (c) standard threshold approach and (f) synergy approach applied at site #9 on 22th. (g) and (h) standard threshold approach and (i) and (j) synergy approach applied at site #5 on 16th and 17th respectively.

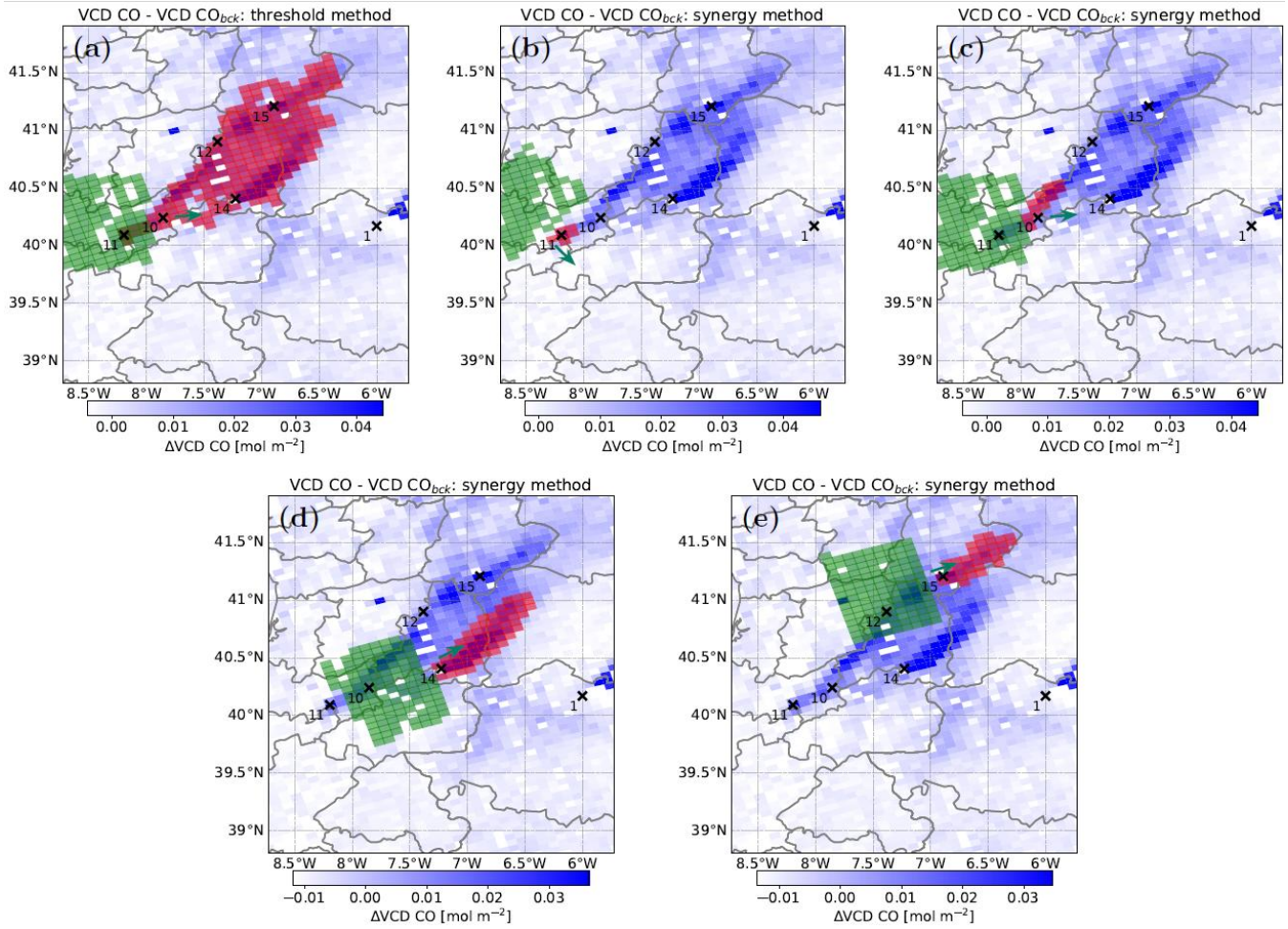


Figure S16: Representative background-corrected CO VCD (ΔCO) for TROPOMI overpass on 17th August 2025. (a) After applying the standard threshold plume masking method at point of interest #10. The rest of the panels correspond to ΔCO after applying the synergy plume masking at the point of interest (b) #11. (c) #10. (d) #14. (e) #15.

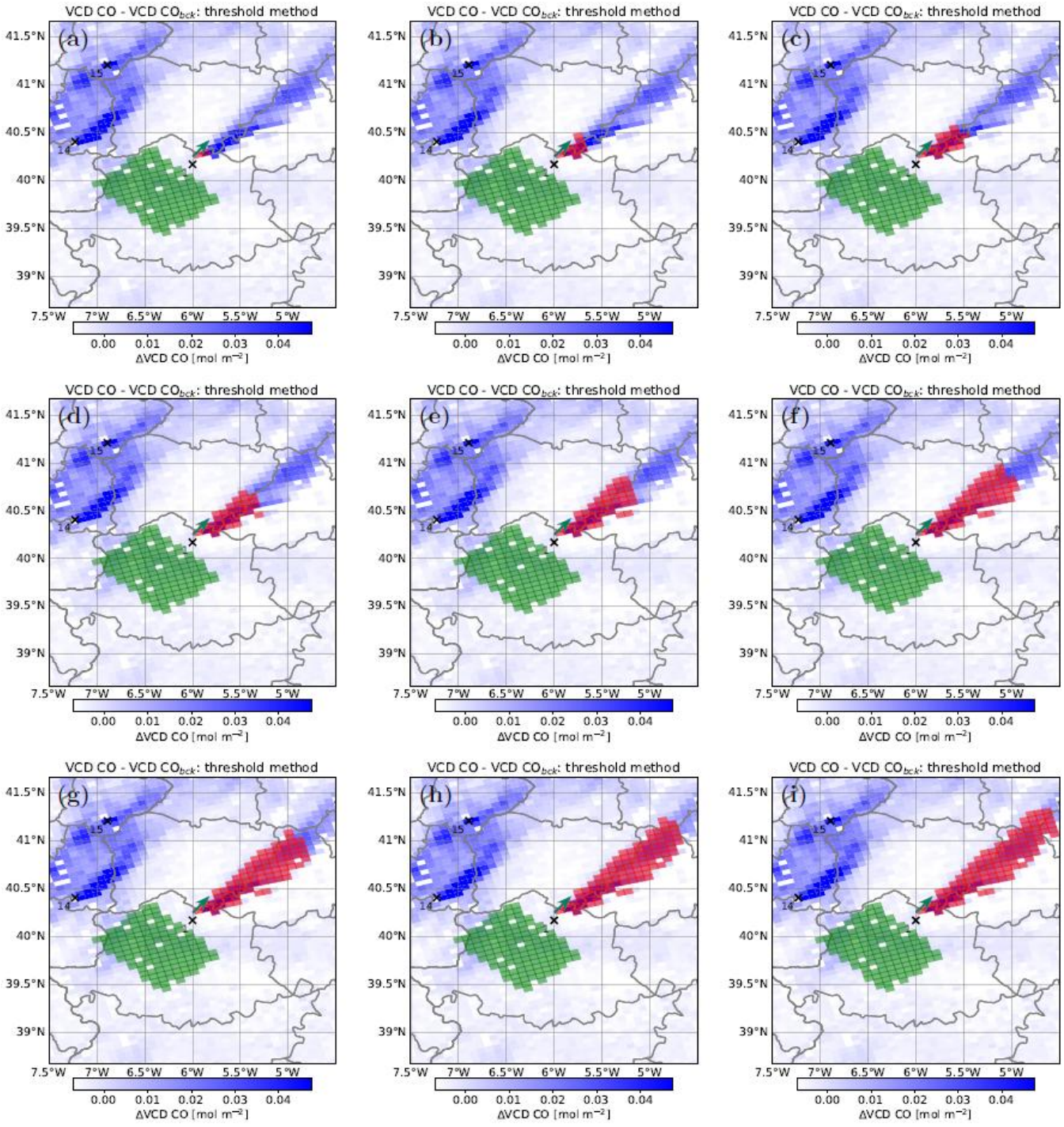


Figure S17: Background-corrected CO VCD maps (ΔCO VCD) after applying the standard threshold plume masking method at site #1 on 17th August, with different distance thresholds: (a) 0.2º (b) 0.4º (c) 0.6º (d) 0.8º (e) 1.0º (f) 1.2º (g) 1.4º (h) 1.6º (i) 1.8º.

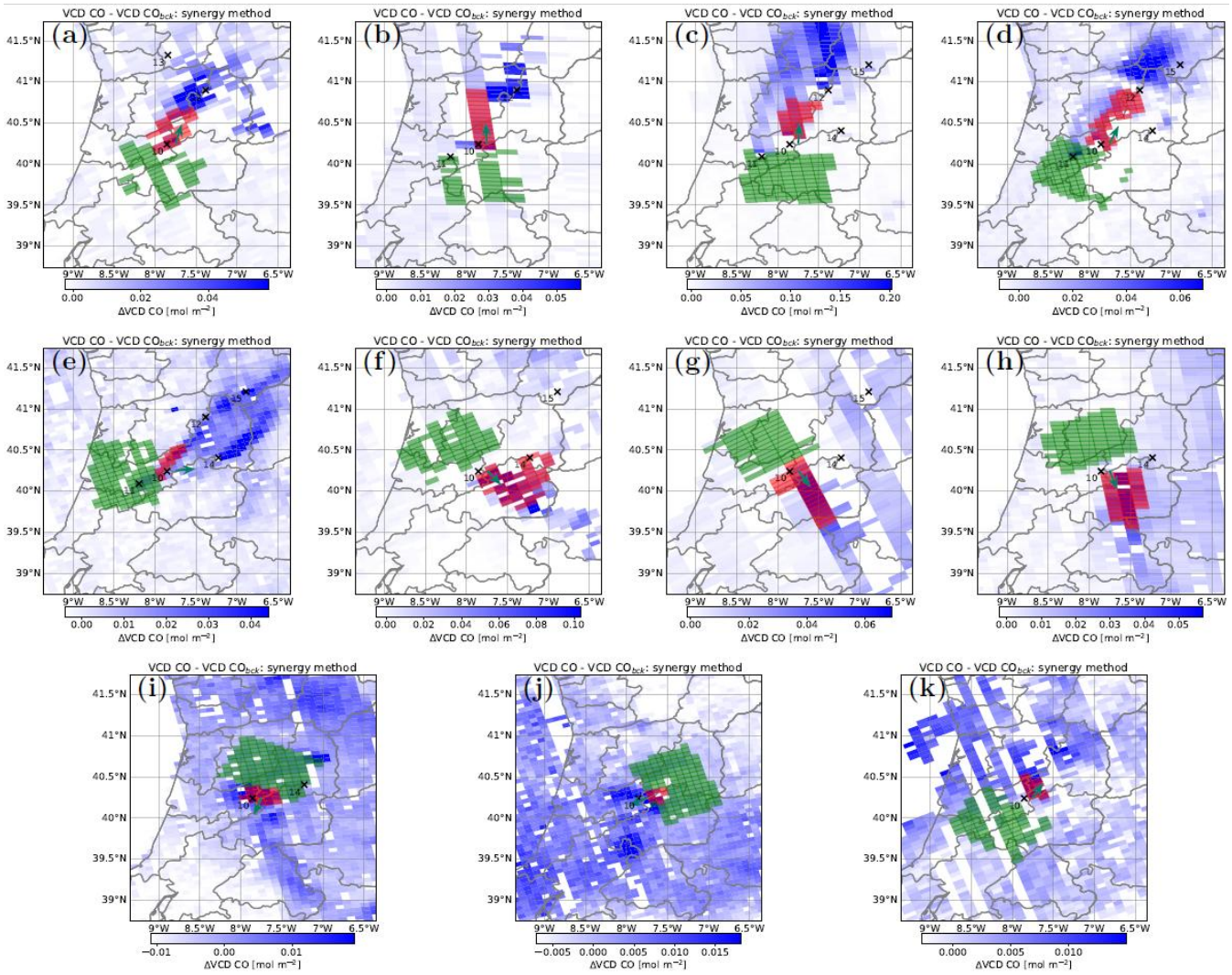


Figure S18: Background-corrected CO VCD maps (ΔCO VCD) after applying the synergy plume evolution associated to #10 wildfire. Each panel correspond to TROPOMI overpass on one day, from 13th (a) to 23th (k) August 2025.

References

Beirle, S., Boersma, K. F., Platt, U., Lawrence, M. G., and Wagner, T.: Megacity Emissions and Lifetimes of Nitrogen Oxides Probed from Space, Science, 333, 1737–1739, https://doi.org/10.1126/science.1207824, 2011.

Finch, D. P., Palmer, P. I., and Zhang, T.: Automated detection of atmospheric NO2 plumes from satellite data: a tool to help infer anthropogenic combustion emissions, Atmospheric Measurement Techniques, 15, 721–733, https://doi.org/10.5194/amt-15-721-2022, 2022.

Griffin, D., McLinden, C. A., Dammers, E., Adams, C., Stockwell, C. E., Warneke, C., Bourgeois, I., Peischl, J., Ryerson, T. B., Zarzana, K. J., Rowe, J. P., Volkamer, R., Knote, C., Kille, N., Koenig, T. K., Lee, C. F., Rollins, D., Rickly, P. S., Chen, J., Fehr, L., Bourassa, A., Degenstein, D., Hayden, K., Mihele, C., Wren, S. N., Liggio, J., Akingunola, A., and Makar, P.: Biomass burning nitrogen dioxide emissions derived from space with TROPOMI: Methodology and validation, Atmospheric Measurement Techniques, 14, 7929–7957, https://doi.org/10.5194/amt-14-7929-2021, 2021.

Griffin, D., Chen, J., Anderson, K., Makar, P., McLinden, C. A., Dammers, E., and Fogal, A.: Biomass burning CO emissions: exploring insights through TROPOMI-derived emissions and emission coefficients, Atmospheric Chemistry and Physics, 24, 10 159–10 186, https://doi.org/10.5194/acp-24-10159-2024, 2024.

Huang, R. and Wang, S.: Global variability in the detectability of power plant NO2 plumes from space, EGUsphere, 2026, 1–51, https://doi.org/10.5194/egusphere-2025-6008, 2026.

Krol, M., van Stratum, B., Anglou, I., and Boersma, K. F.: Evaluating NOx stack plume emissions using a high-resolution atmospheric chemistry model and satellite-derived NO2 columns, Atmospheric Chemistry and Physics, 24, 8243–8262, https://doi.org/10.5194/acp-24-8243-2024, 2024.

Lauvaux, T., Giron, C., Mazzolini, M., d'Aspremont, A., Duren, R., Cusworth, D., Shindell, D., and Ciais, P.: Global assessment of oil and gas methane ultra-emitters, Science (New York, N.Y.), 375, 557–561, https://doi.org/10.1126/science.abj4351, 2022.

Novelli, P. C., Masarie, K. A., and Lang, P. M.: Distributions and recent changes of carbon monoxide in the lower troposphere, Journal of Geophysical Research: Atmospheres, 103, 19 015–19 033, https://doi.org/10.1029/98JD01366, 1998.

Schuit, B. J., Maasakkers, J. D., Bijl, P., Mahapatra, G., van den Berg, A.-W., Pandey, S., Lorente, A., Borsdorff, T., Houweling, S., Varon, D. J., McKeever, J., Jervis, D., Girard, M., Irakulis-Loitxate, I., Gorroño, J., Guanter, L., Cusworth, D. H., and Aben, I.: Automated detection and monitoring of methane super-emitters using satellite data, Atmospheric Chemistry and Physics, 23, 9071–9098, https://doi.org/10.5194/acp-23-9071-2023, 2023